JOURNAL OF COMPUTATIONAL PHYSICS 114, 85–99 (1994)

On the Origin of Parasitic Modes in Numerical Modelling of Wave Propagation in Plasmas

MIKKO J. ALAVA AND JUKKA A. HEIKKINEN*

Helsinki University of Technology, Department of Technical Physics, FIN-02150, Espoo, Finland

AND

TORBJÖRN HELLSTEN

Royal Institute of Technology, Alfvén Laboratory, S-10044, Stockholm, Sweden

Received November 4, 1992; revised February 4, 1994

The mode mixing encountered in solving the boundary value problem arising in studies of wave propagation in hot one-dimensional plasmas is investigated. The wave differential equations, second order in ion Larmor radius, are shown to contain close to the ion cyclotron resonance an unwanted coupling mechanism, closely related to mode conversion driven by the equilibrium gradients. Consequently, the solution mixes with parasitic modes which carry power out of the resonance zone. In the case of strong coupling, this may lead to a generation of excess energy flux for complex valued coefficients of the wave equations. The importance and effects of this phenomenon are demonstrated in the special case of simulations of minority ion cyclotron heating in tokamaks. It is shown that the mode mixing can be avoided by adjusting the elements of the coefficient matrix of the wave equations, which makes the second-order system amenable to the problems with high minority concentration which is important for studies of fusion physics.

1. INTRODUCTION

The solution of wave propagation, absorption, and coupling is an important branch of computational plasma physics, especially because of its close connection with the heating of fusion plasmas. The problem consists of solving the appropriate in-time Fourier-analyzed wave equations as a boundary value problem in one, two, or even three dimensions. Assuming that a constitutive relation for the plasma has been derived, the equations are of the form

$$\nabla \times \nabla \times \mathbf{E} = i\omega\mu_0 \mathbf{j}_{\text{ext}} - \frac{\omega^2}{c^2} \boldsymbol{\varepsilon} \cdot \mathbf{E}, \tag{1}$$

where $\mathbf{E}$ is the electric field vector in the plasma, ω is the angular frequency of the wave. $\mathbf{j}_{\text{ext}}$ stands for the externally applied currents and $\boldsymbol{\varepsilon}$ is the dielectric tensor of the medium. In an inhomogeneous hot plasma $\boldsymbol{\varepsilon}$ is an integral operator. To make the problem tractable we assume the plasma to be sufficiently homogeneous so that the differential operator formulation for the dielectric tensor can be used. From this starting point, one can proceed for geometries having one or two ignorable directions by Fourier-decomposing the periodic spatial dimensions away and by making simplifying assumptions about the dielectric properties of the medium [1].

Although the basic equation (1) looks rather simple at first glance, its solution is known to be very cumbersome. The reason lies in the fact that the corresponding dispersion relation often yields more than one propagating mode. Fortunately, in most cases the modes have vastly different wavenumbers and can therefore be separated fairly easily. However, for certain conditions the different wave branches interact, e.g., at mode conversion layer or at steep gradients, which complicates the problem. For wave propagation in a plasma slab one is often interested in transmission, mode conversion, and absorption coefficients. Hence, there is a need to calculate how much power is transferred from one branch to another. The power balance calculation requires the decomposition of the wave field to all branches at appropriate points, e.g., at the boundaries.

The ensuing system can be solved numerically with finite difference (FD) methods [2] or with finite element (FEM) techniques [3, 4]. In one dimension both give accurate results although with problems of their own concerning computer time, memory requirements, or numerical pollution in the solution due to ill-posedness of the operator $\nabla \times \nabla \times$ [5]. For these reasons, solving the wave propagation problem in full 3D geometry is a difficult task due to the natural restrictions of the method: memory space in FEM and slowness of convergence in FD schemes. One concern is

* Permanent address: VTT Energy, PO Box 1606, FIN-02044 VTT, Finland.

0021-9991/94 $6.00

that the wave equation system is an approximative one, depending on how the response of the plasma has been dealt with. The absorption of the wave mode can be calculated quantitatively only by using the hot plasma description of the plasma. This means usually a development of the plasma dielectric tensor to second order in the parameter $k_\perp r_i$, where $k_\perp$ is the mode wave vector perpendicular to the magnetic field and r_i is the ion Larmor radius [6]. The ensuing differential equations are commonly called finite Larmor radius (FLR) equations.

The Larmor radius expanded equations suffer from problems due to the fact that outside the mode conversion regions only the wavelength of the fast magnetosonic wave remains usually long enough to satisfy the condition $k_\perp^2 r_i^2 \ll 1$. For the commonly used second-order expansion this will not only give rise to an incorrect dispersion relation for the short wavelength modes but also to unphysical effects like negative absorption. To overcome the failure of the FLR equations, one may, e.g., use artificial damping [7] in order to reduce the effect of the short wavelength modes on the absorption, reflection, and transmission of the long wavelength fast wave. Such methods are, however, cumbersome to use and do not take into account the origins of the problem. One should note that a general wave solution using a correct development of the plasma response to arbitrary order in $k_\perp r_i$ leads to a system of integrodifferential equations [9, 10]. Their solutions pose a challenging computational and physical problem that has been attempted to deal with only recently by Sauter and Vaclavik [9, 11].

In this paper, we analyse some of the problems arising in solving the second-order FLR equations in a situation where they do not give the correct dispersion for all the plasma modes. We start by considering simplified second-order wave equations which have a similar resonance as the complete equations. The analytical solution of the model equations and their numerical analysis connects the present subject to a broader context, beyond plasma physics. It is shown how the mechanism of gradient conversion [12] can lead to a coupling between the long and short wavelength modes. This can occur also when the dispersion of the propagating short wavelength mode is not described correctly in the proximity of the resonance layer. This particular, unphysical case is an example of the more general situation where the real part of the highest order coefficient $\mathrm{Re}[\sigma]$ of the wave equations has a zero or resonance. In the case of the FLR equations, this behaviour occurs for a minority heating scenario in which the charge to mass ratio of the minority ion species is not equal to that of the majority ion species. Given a high enough minority concentration, two zeros of $\mathrm{Re}[\sigma]$ can exist: one at the cyclotron resonance layer and one on the high field side [13].

We show by analytical means how the strength of the gradient conversion depends on the boundary conditions by separating the field into the wave components at the boundaries. The analytical results are then compared with numerical calculations using a simplified wave equation that is appropriate for the study of the creation of the short wavelength mode from the process. These studies are complemented by outlining what happens if a complete set of wave equations is used in a slab geometry with comparable plasma parameters. A further failure of the second-order equations occurs at the description of absorption of the left-handed field component. It not only gives the wrong magnitude but also the wrong sign. To avoid the problem with the left-handed component, which is enhanced at the fundamental cyclotron resonance and becomes strongly emphasized for large minority concentrations, we consider means to modify the wave equations. By changing the second-order corrections to the coefficients of the wave equations such that the negative absorption vanishes we are able to reduce the mode mixing significantly. With this easy-to-implement approach, we are able to analyze the physics of fast wave heating and mode conversion without the problems stemming from the failure of the FLR expansion.

This paper is constructed in the following way. Section 2 presents the wave equations and the analytical theory, together with evidence from a numerical solution of the reduced wave equation. In Section 3 we continue with the study of the full wave equations. The effect of mode mixing on the energy balance and the relative mode amplitudes is analysed. We discuss methods by which the dispersion can be changed so as to reach correct results. Section 4 finishes the paper by the conclusions.

2. PHYSICAL BACKGROUND

2.1. Negative Absorption

For homogeneous plasmas, the dielectric tensor has been developed to all orders in the ion Larmor radius. For a Maxwellian velocity distribution one has [6]

$$\varepsilon_{ij} = \delta_{ij} - \sum_\alpha \frac{\omega_{p\alpha}^2}{\omega^2} \left\{ - \sum_{n=-\infty}^{\infty} a_{0\alpha} \Pi_{\alpha ij}(\beta_\alpha a_{n\alpha}; n) \times Z(a_{n\alpha}) - a_{0\alpha}^2 \hat{z}\hat{z} \right\}, \tag{2}$$

where

$$a_{n\alpha} = \frac{1 - n\Omega_\alpha/\omega}{n_z v_{T\alpha}/c} \tag{3}$$

and Z denotes the complex-valued plasma dispersion function and summation extends over all particle species. $v_{T\alpha}$, $\omega_{p\alpha}$, and Ω_α are the thermal velocity $\sqrt{2T_\alpha/m_\alpha}$, plasma frequency, and cyclotron frequency of the αth species ($\alpha = e$,

for electrons), respectively. T_α is the temperature (in energy units) of the αth species and m_α is the corresponding mass. n_z and $\hat{z}$ are the refractive index of the wave and the unit vector, respectively, in the direction of the background magnetic field. In considering the finite Larmor radius effects on the wave absorption we need the perpendicular components ($i, j = x$ or y) of the matrix Π with respect to the magnetic field. These are given by

$$\Pi_{(\alpha xy)} = \begin{pmatrix} \frac{n^2}{\beta_\alpha} \Lambda_n(\beta_\alpha) & in\Lambda_n'(\beta_\alpha) \\ -in\Lambda_n'(\beta_\alpha) & \frac{n^2}{\beta_\alpha} \Lambda_n(\beta_\alpha) - 2\beta_\alpha \Lambda_n'(\beta_\alpha) \end{pmatrix}, \quad (4)$$

where $\beta_\alpha = k_\perp^2 v_{T\alpha}^2 / 2\Omega_\alpha^2$ and $\Lambda_n(\beta_\alpha) = I_n(\beta_\alpha) \exp(-\beta_\alpha)$. I_n is the modified Bessel function of the nth order.

One problem which appears with the second-order approximation in the Larmor radius over the wavelength is that the energy absorption becomes negative. This is not physically relevant and causes problems in the numerical codes. The problem can be illustrated by studying wave absorption in a homogeneous plasma. With the dielectric tensor given in Eq. (2), the absorbed power density is obtained from $p = \varepsilon_0 \omega \operatorname{Im}(\mathbf{E}^* \cdot \varepsilon \cdot \mathbf{E})$. By transforming the coordinates so that the base vectors coincide with the eigenvectors $\hat{e}_i$ of the anti-Hermitian part of the tensor ε we have

$$p = \varepsilon_0 (\omega_{p\alpha}^2/\omega)\, a_{0\alpha} \operatorname{Im}[Z(a_{n\alpha}](\mu_1 |E_1|^2 + \mu_2 |E_2|^2), \quad (5)$$

where μ_i, $i = 1, 2$, are the eigenvalues and $\mathbf{E} = E_1 \hat{e}_1 + E_2 \hat{e}_2$. In Fig. 1, we show the eigenvalues μ_i as a function of β_α corresponding to the fundamental cyclotron resonance of the species α, i.e., by considering only the term $n = 1$ in Eq. (2). Both eigenvalues are positive which means that the absorption is positive, too. When expanding Π to second order in the ion Larmor radius, i.e., to first order in β_α, one obtains

$$\Pi_{\alpha(xy)}^{(1)} = \begin{pmatrix} \frac{1-\beta_\alpha}{2} & \frac{i(1-2\beta_\alpha)}{2} \\ -\frac{i(1-2\beta_\alpha)}{2} & \frac{1-3\beta_\alpha}{2} \end{pmatrix}. \quad (6)$$

The eigenvalues to $\Pi^{(1)}$ are given by $\tilde{\mu}_{1,2} = (1-2\beta_\alpha)/2 \pm \frac{1}{2}\sqrt{1-4\beta_\alpha+5\beta_\alpha^2}$ and are plotted in Fig. 1. For small β_α the corresponding eigenvectors coincide with the rotating electric field components $E_\pm = E_x \pm iE_y$. As we can see, one of the eigenvalues becomes negative. Again, at low values of β_α, $\tilde{\mu}_2$ is small as compared to $\tilde{\mu}_1$. What makes things worse is that near the cyclotron resonance we have, except for small minority concentrations of the resonating ion species,

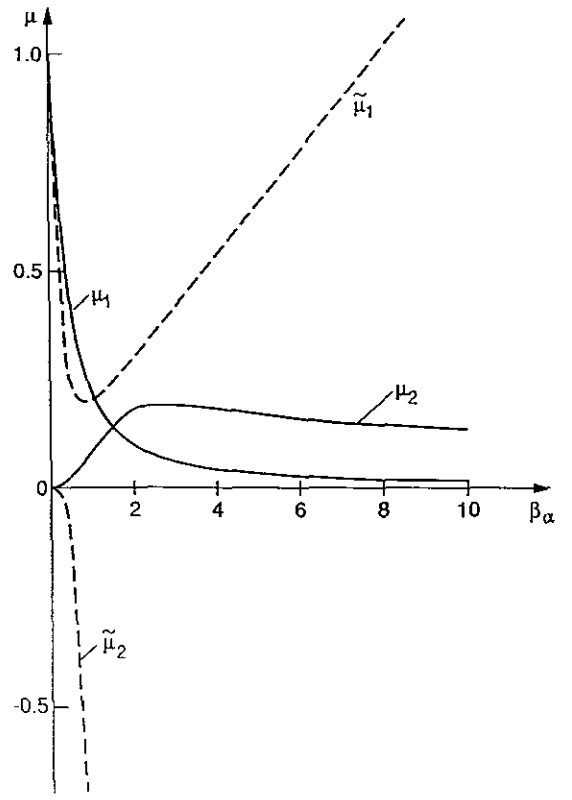

FIG. 1. The eigenvalues of the tensors in Eqs. (4) (solid curve) and (6) (dashed curve) as a function of β_α.

that $|E_-| \gg |E_+|$ for the fast wave while the eigenvector corresponding to $\tilde{\mu}_2$ coincides with E_-. Therefore, this problem becomes, in principle, severe for heating at the fundamental ion cyclotron frequency with large minority concentrations for which $|E_-|/|E_+|$ becomes large. In practice the sign of the absorption is determined by the total electric field, which may consist of other modes, in addition to a single fast wave, leading to a much more complicated situation.

For $n = 2$, the second-order expansion leads to positive eigenvalues and there is formally no problem except that ensuing from the inaccuracy of the second-order expansion. This, however, is valid only for small β_α. Thus, only the magnetosonic wave can be properly described by the code and the short wavelength modes only near the mode conversion layers, close to which β_α is locally small. Therefore, the absorption profiles based on the damping of the ion Bernstein wave (IBW) or kinetic Alfvén wave may not be accurate.

2.2. Wave Equations

The wave equations to second order in the ion Larmor radius in an inhomogeneous plasma can be found in Refs. [14, 15], where their derivation is also given. Here, neglect-

ing magnetic shear and toroidicity, we write the wave equations for $n_y = 0$ in a reduced form,

$$-[(\sigma_2-\sigma_1)\,E_x']' + i[(\delta_2-2\delta_1)\,E_y']' + (n_z^2-S)\,E_x + iDE_y + in_zE_z' = 0 \tag{7}$$

$$-i[(\delta_2-2\delta_1)\,E_x']' - [(\sigma_2-3\sigma_1+2\lambda_0)\,E_y']' - iDE_x - E_y'' + (n_z^2-S)\,E_y + n_z(\xi_0 E_z)' = 0 \tag{8}$$

$$-n_z\xi_0 E_y' + in_zE_x' - E_z'' - PE_z = 0, \tag{9}$$

where E_x, E_y, and E_z denote the electric field components perpendicular to the magnetic field (x, y) and in the direction of it (z), respectively. The prime denotes the derivative with respect to x; n_z and n_y are the corresponding refractive indices of the radiation. A plasma slab inhomogeneous in the radial direction (x) is assumed. Equations (7)–(9) include finite temperature and finite electron inertia effects and allow arbitrary profiles for the equilibrium parameters. A number of unimportant kinetic corrections as well as terms proportional to second derivatives of the coefficients have been left out of the equations. In their present form, the essential features of the electrostatic wave excitation by the equilibrium gradients and various resonances can be described [16, 17].

The dielectric tensor elements are given by

$$S = 1 + \sum_i \kappa_i [Z(a_{1i}) + Z(a_{-1i})] \tag{10}$$

$$D = -\sum_i \kappa_i [Z(a_{1i}) - Z(a_{-1i})] - \frac{\omega_{pe}^2}{\Omega_e \omega} \tag{11}$$

$$P = 1 - \left(\frac{\omega_{pe}^2}{\omega^2}\right) a_{0e}^2 Z'(a_{0e}) \tag{12}$$

$$\sigma_n = \lambda_{-n} + \lambda_n \tag{13}$$

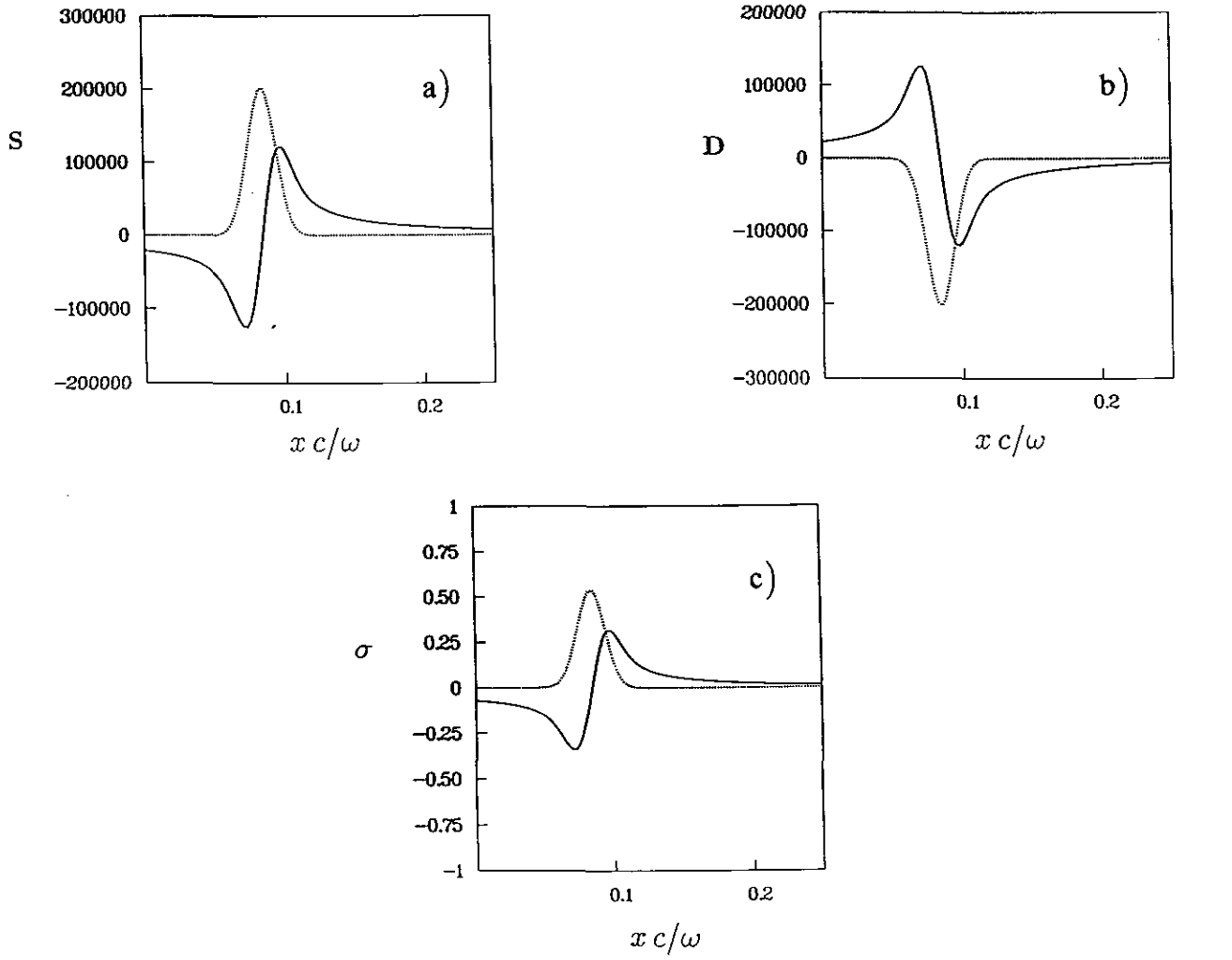

FIG. 2. The behaviour of (a) S, (b) D, and (c) σ around the cyclotron resonance as a function of xc/ω. The cyclotron resonance layer ($\omega = \Omega_D$) is located at $x = 0.085$ m. A tritium-deuterium plasma with 50% relative concentrations. The magnetic field (B_0) at the resonance is 3 T, $\omega = 1.4325 \times 10^8\ \mathrm{s}^{-1}$ corresponding to the cyclotron frequency Ω_D of deuterium at the resonance, $n_z = 2$, $n_y = 0$, $n_e = 5 \times 10^{19}\ \mathrm{m}^{-3}$ and $T = 5$ keV.

$$\delta_n = \lambda_{-n} - \lambda_n \tag{14}$$

$$\lambda_n = -\sum_i \kappa_i r_i^2 Z(a_{ni}) \tag{15}$$

$$\xi_n = \sum_i \kappa_i r_i^2 a_{0i} Z'(a_{ni}), \tag{16}$$

where

$$\kappa_i = \frac{\omega_{pi}^2 c}{2\omega^2 n_z v_{Ti}}, \tag{17}$$

and the summation extends over all ion species. All the lengths are normalised to c/ω; r_i denotes the ion Larmor radius $(v_{Ti}/\sqrt{2}\,c)(\omega/\Omega_i)$.

The kinetic effects are introduced via the terms proportional to σ_n, δ_n, λ_n, and ξ_n, while the finite electron inertia effects are equivalent to including E_z in the equations, i.e., having finite P. Equations (7)–(9) reduce to

$$E_y'' + \frac{(S-n_z^2)^2 - D^2}{S-n_z^2} E_y = 0 \tag{18}$$

in the limit $|P| \to \infty$ and $\sigma_n, \delta_n, \lambda_n, \xi_n \to 0$ as can be seen by putting $E_z = 0$ and $\sigma_n, \delta_n, \lambda_n, \xi_n = 0$ and by solving Eq. (7) for E_x and substituting it into Eq. (8).

2.3. Wave Branches

Equations (7)–(9) support three different modes which in typical plasma applications in the ion cyclotron range of frequencies have greatly differing wavenumbers, corresponding to a fast magnetosonic wave, a slow wave, and an ion Bernstein wave or a kinetic Alfvén wave. Consequently, they propagate independently and are damped whenever $|a_{ji}|$ approaches or becomes comparable to unity for ions or electrons, in which case $Z(a_{ji})$ has a nonzero complex part (for nonzero n_z). Around the regions, where $S - n_z^2$ has a zero, the wavenumbers of two different modes coalesce and the corresponding modes become coupled [8]. In this case, the power flux of the magnetosonic wave is converted to that the electrostatic waves, or vice versa. The conversion may also take place with steep equilibrium gradients [19] when the inverse gradient lengths approach the value of the electrostatic wave wavenumber. It has been shown that these mechanisms can be well described by a local analysis [16, 12].

In the present study, we concentrate on the wave behaviour near the zeros or singularities of $\mathrm{Re}[\sigma]$, where Re denotes the real part of the expression inside the brackets and $\sigma = \sigma_2 - \sigma_1$. These special points appear, e.g., at the zeros of a_{ji}, i.e., at the cyclotron harmonic resonances $\omega = j\Omega_i$; $j = \pm 1, \pm 2$. For $n_z = 0$, σ has a singularity at $\omega = \Omega_i$, while for $n_z \neq 0$, $\mathrm{Re}[\sigma]$ has a zero there. In a multi-ion component plasma, σ may also have a zero between two separate cyclotron resonances. Figure 2 shows σ, S, and D as a function of x around the cyclotron resonance for typical tokamak plasma parameters. We have taken the constant density and temperature while the magnetic field is assumed to vary as $B_0/(1 - x/R_0)$, where R_0 denotes the major radius at the cyclotron resonance. The plasma is composed of deuterium and tritium with equal proportions. At the special points mentioned above the finite Larmor radius expansion is not valid. While the magnetosonic wave propagation is well described over these points, Eqs. (7)–(9) fail in describing the short wavelength kinetic mode. Figure 3 shows the wavenumbers of the three modes as a function of x around the cyclotron resonance as deduced from Eqs. (7)–(9). The parameters are the same as in Fig. 2. According to the exact dispersion relation [8], the shortest wavelength mode propagates only on the low field side of the cyclotron resonance in the depicted region, while Eqs. (7)–(9) have a propagating root, corresponding to the ion Bernstein wave branch, on both sides of the resonance. As it will be shown later, the fact that the ion Bernstein wave propagates with oppositely directed energy fluxes on both sides of the resonance leads to ill-defined problems in a finite plasma.

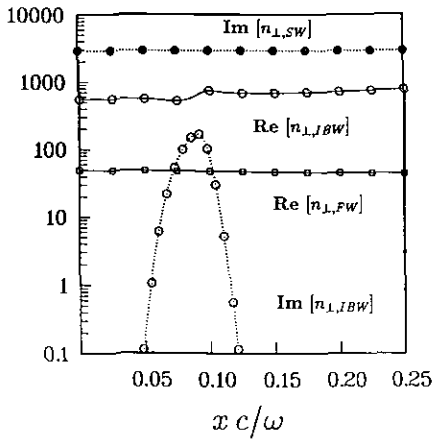

FIG. 3. The wavenumbers of the modes around the resonance calculated from Eqs. (7)–(8). The resonance layer is at $x = 0.085$ m. The real parts have been drawn with solid lines, the imaginary parts with dotted ones. Solid circles denote the slow wave root, open ones the ion Bernstein root and open squares the fast wave root. The real part of the slow wave root is very small. The sign of the IBW root has been chosen so that $\mathrm{Re}[n_\perp] > 0$.

2.4. Simplified Examples

To show that the special points of σ can be a serious source of unwanted modes, we discuss a simplified case of Eqs. (7)–(9) with $n_z = 0$. Consider the model profiles $\sigma = 1/x$, $S = \kappa/x$, and $D = -\kappa(1/x + \alpha)$, which roughly simulate the true behaviour of the dielectric tensor elements around the cyclotron resonance with $n_z = 0$. In the case of large κ, the short wavelength mode is described by Eq. (7),

and E_y can be assumed to be a given constant around the resonance (the latter approximation has been found useful for analysing mode conversion at $S=n_z^2$ resonances; its validity in the present case is usually not as good). Note that this assumption is equivalent to considering the electrostatic mode being driven by a constant amplitude fast wave. From Eq. (7), we find that

$$xE'' - E' + \kappa x E = -i\kappa E_y \alpha x^2 \equiv Fx^2, \tag{19}$$

where we have used the transformation $E_x \to E - iE_y$. Equation (19) has a solution,

$$\begin{aligned} E = {} & AxJ_1(\sqrt{\kappa}\,x) + BxY_1(\sqrt{\kappa}\,x) \\ & + \frac{\pi}{2} Fx \Big[Y_1(\sqrt{\kappa}\,x) \int^x J_1(\sqrt{\kappa}\,x)\, x\, dx \\ & - J_1(\sqrt{\kappa}\,x) \int^x Y_1(\sqrt{\kappa}\,x)\, x\, dx \Big], \end{aligned} \tag{20}$$

where J_1 and Y_1 denote the first-order Bessel functions and the constants A and B are determined by the boundary conditions. To determine the unknown coefficients A and B, the outward radiating boundary conditions are placed far away from the resonance, i.e.,

$$\begin{aligned} & E \to C_+ x[J_1(\sqrt{\kappa}\,x) + iY_1(\sqrt{\kappa}\,x)] + Fx/\kappa; \qquad x \to \infty \\ & E \to C_- x[J_1(\sqrt{\kappa}\,x) + iY_1(\sqrt{\kappa}\,x)] + Fx/\kappa; \qquad x \to -\infty, \end{aligned} \tag{21}$$

where the unknowns C_+ and C_- determine the amplitudes of the outward emanating short wavelength modes. Note that in our applications $\mathrm{Im}[\sigma E_x^* E_x']$ corresponds to the physical energy flux of the short wavelength mode in the context of Eq. (19). Hence, the mode is a forward mode ($v_{ph} v_g > 0$) for positive x and a backward wave ($v_{ph} v_g < 0$) for negative x. Here v_{ph} and v_g are the phase velocity and group velocity of the mode, respectively. This yields the correct choice of the signs in front of Y_1 in the boundary conditions in Eq. (21). Applying these conditions for the solution in Eq. (20), we find the constraint

$$\begin{aligned} & i\Big[A - \frac{\pi}{2} \frac{F}{\sqrt{\kappa}} \int_w^\infty Y_0(\sqrt{\kappa}\,x)\, dx \Big] \\ & \quad = B + \frac{\pi}{2} \frac{F}{\sqrt{\kappa}} \int_w^\infty J_0(\sqrt{\kappa}\,x)\, dx, \end{aligned} \tag{22}$$

but A and B remain otherwise undetermined. This example shows how such boundary conditions as in Eq. (21) can make the problem ill-defined in the case where the short wavelength mode propagates on both sides of the resonance with opposite power flux directions. An analogous case is the second-order differential equation $E'' + \kappa E = 0$ with a constant κ and with the boundary conditions $E \propto \exp(i\sqrt{\kappa}\,x)$ on both left and right boundaries. Although the problem presented above could be anticipated to be difficult to handle numerically, this is usually not the case. With a bounded calculation region and with boundary conditions not identical to the infinite-case solution, A and B can always be determined for the solution in Eq. (20).

As another example we take the model profiles $\sigma = ax + i\rho$, $S = \kappa\sigma$, and $D = -\kappa(\sigma + \alpha)$. These simulate the behaviour of the dielectric tensor elements around the resonance for $n_z \neq 0$. We take a, ρ, κ, and α as constants and assume that $S - n_z^2 \simeq S$ and $E_z = 0$ to simplify the analysis. As in the previous example, E_y is assumed to be constant, and we find from Eq. (7) that

$$[(ax + i\rho)\, E']' + \kappa(ax + i\rho)\, E = -i\kappa\alpha E_y \equiv Fa^2 \tag{23}$$

after the transformation $E_x \to -iE_y + E$. Equation (23) has the solution

$$\begin{aligned} E = {} & AJ_0(\sqrt{s}\,z) + BY_0(\sqrt{s}\,z) \\ & + \frac{\pi}{2} F \Big[Y_0(\sqrt{s}\,z) \int^z J_0(\sqrt{s}\,z)\, dz \\ & - J_0(\sqrt{s}\,z) \int^z Y_0(\sqrt{s}\,z)\, dz \Big], \end{aligned} \tag{24}$$

where J_0 and Y_0 denote the Bessel functions of order zero, $z = ax + i\rho$, and $s = \kappa/a^2$. Again, the outward radiating boundary conditions at infinity leave A and B undetermined, but for a bounded calculation region they can be determined. To show this, we assume the boundaries at $x = \pm L$ and set the conditions

$$\begin{aligned} E &= -i\alpha E_y/p + C_+ \\ E' &= i\sqrt{\kappa}\, C_+ \end{aligned} \tag{25}$$

at $x = L$, and

$$\begin{aligned} E &= -i\alpha E_y/q + C_- \\ E' &= i\sqrt{\kappa}\, C_- \end{aligned} \tag{26}$$

at $x = -L$. Here we have used the notations $p = aL + i\rho$ and $q = -aL + i\rho$, and C_+ and C_- are the unknown amplitudes of the emanating short wavelength modes. The latter are assumed to have a dependence $\exp(i\sqrt{\kappa}\,x)$ at the bound-

aries. By applying these conditions to the solution in Eq. (24), we find that

$$\begin{aligned} Aq_1 + Bq_2 &= \frac{\alpha E_y}{p} - \frac{\pi}{2} F\left[q_2 \int^p J_0(\sqrt{s}\, z)\, dz \right. \\ &\quad \left. - q_1 \int^p Y_0(\sqrt{s}\, z)\, dz \right] \\ Aq_3 + Bq_4 &= \frac{\alpha E_y}{q} - \frac{\pi}{2} F\left[q_4 \int^q J_0(\sqrt{s}\, z)\, dz \right. \\ &\quad \left. - q_3 \int^q Y_0(\sqrt{s}\, z)\, dz \right], \end{aligned} \tag{27}$$

where $q_1 = iJ_0(\sqrt{s}\, p) - J_0'(\sqrt{s}\, p)$, $q_2 = iY_0(\sqrt{s}\, p) - Y_0'(\sqrt{s}\, p)$ and with the same definitions for q_3 and q_4, respectively, but with q substituted for p. The prime denotes here the derivation with respect to the argument of the Bessel function.

From Eqs. (27), A and B can be determined algebraically, and C_+ and C_- can then be obtained from Eqs. (25) and (26). Figure 4 shows $E'(x)$ calculated numerically from Eq. (23) with a finite element discretization and using the boundary conditions shown in Eqs. (25) and (26). We have taken $a = 30$, $L = 0.025$, $\kappa = 300{,}000$, $\alpha = 0.001$, $\rho = 0.01$, and $E_y = 1$. The result shows a short wavelength mode which emanates from $x = 0$ towards both boundaries. C_+ and C_- are found to be complex conjugates, and $C_+ = -0.0055 - i0.0132$. The result agrees accurately with the analytical prediction, thus proving that the parasitic coupling is not of numerical origin, but that it is a consequence of the particular boundary conditions at $x = \pm L$ and of the equilibrium gradients of σ, S, and D.

We note that with $\alpha = 0$, $C_+ = C_- = 0$ according to the analytical result. This fact, as well as the proportionality of C_+ and C_- to α and E_y, is accurately reproduced by the numerical code. As we have stressed earlier, Eqs. (7)–(9) do not describe the short wavelength mode correctly around the cyclotron resonance or zeros of σ. This frees us from discussing the physical origin of the coupling. To understand its mathematical origin more thoroughly we write the energy conservation law from Eq. (7) with n_z small and constant E_y as

$$I' + Q = 0, \tag{28}$$

where $I = \mathrm{Im}[\sigma E_x^* E_x']$ denotes the energy flux of the short wavelength mode and $Q = \mathrm{Im}[S]\,|E_x|^2 - \mathrm{Im}[iDE_x^* E_y] - \mathrm{Im}[\sigma]\,|E_x'|^2$ includes the dissipation and a coupling term between E_x and E_y. We note that the imaginary parts of S and σ are always positive from Eqs. (10) and (13). Hence, the magnitude of σ can affect the sign of Q. That Q can be negative is obviously an artifact of the finite Larmor radius expansion of the wave equations, discussed in more detail in Section 2.1 and should not appear in the precise theory. Note that the term proportional to $\mathrm{Im}[\sigma]$ gives a nonvanishing contribution also in our example $\sigma = 1/x$ when the Landau integration over the resonance is performed. It is important to note that the coupling term which is proportional to D actually dominates with the parameters in our model examples. This means that we may have parasitic modes even for real coefficients in Eq. (23) ($\rho = 0$) or with other types of boundary conditions which do not correspond to outward radiation of the parasitic modes. This was indeed obtained in our numerical solutions of Eq. (23) for $\rho = 0$ and for $E' = -i\sqrt{\kappa}\, C_-$ instead of $E' = i\sqrt{\kappa}\, C_-$ in the boundary conditions equation (26), and it is evident from our analytical theory. With $\rho = 0$ the converted energy flux, i.e., the change in the energy flux of the short wavelength mode, can be simply calculated from the integral $\int \mathrm{Im}[iDE_x^* E_y]$ over the conversion region.

In the complete system of Eqs. (7)–(9), the energy conservation law Eq. (28) can be written with the definitions

$$\begin{aligned} I &= \mathrm{Im}[E_x^* \sigma E_x' - iE_x^*\, \delta E_y' + iE_y^*\, \delta E_x' + E_y^* \sigma' E_y'] \\ &\quad + \mathrm{Re}[E_y^* B_z - E_z^* B_y] - \mathrm{Im}[n_z \xi_0 E_y^* E_z] \end{aligned} \tag{29}$$

$$\begin{aligned} Q &= \mathrm{Im}[S](|E_x|^2 + |E_y|^2) - \mathrm{Im}[D]\,\mathrm{Im}[E_y^* E_x - E_x^* E_y] \\ &\quad + \mathrm{Im}[P]\,|E_z|^2 - n_z\,\mathrm{Im}[\xi_0]\,\mathrm{Im}[E_z^* B_z] \\ &\quad - \mathrm{Im}[\sigma]\,|E_x'|^2 + \mathrm{Im}[\delta]\,\mathrm{Im}[E_y^{*\prime} E_x' - E_y' E_x^{*\prime}] \\ &\quad - \mathrm{Im}[\sigma']\,|E_y'|^2, \end{aligned} \tag{30}$$

where $B_z = -iE_y'$ and $B_y = n_z E_x + iE_z'$ and we have $\delta = \delta_2 - 2\delta_1$ and $\sigma' = 2\lambda_0 + \sigma_2 - 3\sigma_1$. We find that the total energy flux I remains constant if the dielectric coefficients are real and do not have resonances. It should be remembered nevertheless that conversion to short wavelength modes still exists when equilibrium gradients are present, in which case the increase in the short wavelength wave power

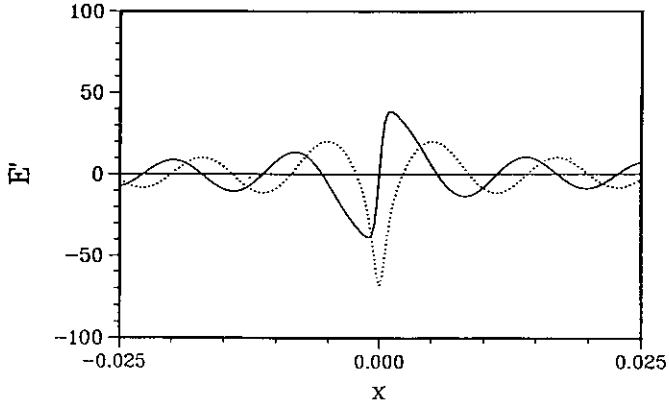

FIG. 4. $E'(x)$ calculated from Eq. (23) for model profiles of S, D, and σ. The boundary conditions are given by Eqs. (25) and (26): $a = 30$, $L = 0.025$, $\kappa = 300{,}000$, $\alpha = 0.01$, $\rho = 0.001$, and $E_y = 1$.

flux equals the loss in the power flux of the magnetosonic wave if $I' = 0$. The phenomenon of the opposite signs of the terms proportional to the imaginary parts of σ and S in Eq. (28) can be seen also in the full conservation law, as noted in Ref. [14]. As will be shown in our numerical examples in Section 3, the term proportional to $\mathrm{Im}[\sigma]$ can in some cases dominate the damping terms around the cyclotron resonance, which means that the total energy flux increases, demonstrating the unphysical nature of that term.

2.5. The Boundary Conditions

Before turning our attention to the solutions of the complete wave equations (2)–(4) we have to discuss the sensitivity of the results to the details of the boundary conditions. It has been shown [3] that Eqs. (7)–(9) can be solved by finite elements. Depending on whether one studies the coupling between the antenna and the plasma or the absorption, transmission, reflection, and conversion one is resorted to different boundary conditions. For the antenna–plasma coupling calculations the global boundary conditions, where the boundaries are set outside the plasma at the tokamak chamber walls, are appropriate. Alternatively, one can solve the equations with local boundaries placed inside the plasma using the outward radiating conditions, which makes it possible to evaluate the scattering coefficients. The goodness of the latter conditions crucially depends on the approximations used to describe the behaviour of the various wave branches on the boundaries lying in the inhomogeneous plasma.

2.5.1. *Wavemode Representation at the Endpoints*

To study the absorption and scattering of the waves around the resonances, we apply the outward radiating conditions and decompose the total wave field $\mathbf{E}$ at the boundaries into three wave branches. The wave field at the endpoints is then described by

$$\mathbf{E} = \tau_f \mathbf{E}_f + \tau_{f\_} \mathbf{E}_{f\_} + \tau_s \mathbf{E}_s + \tau_{s\_} \mathbf{E}_{s\_} + \tau_B \mathbf{E}_B + \tau_{B\_} \mathbf{E}_{B\_} \tag{31}$$

$$\frac{d\mathbf{E}}{dx} = in_{xf} \tau_f \mathbf{E}_f + in_{xf\_} \tau_{f\_} \mathbf{E}_{f\_} + in_{xs} \tau_s \mathbf{E}_s + in_{xs\_} \tau_{s\_} \mathbf{E}_{s\_} + in_{xB} \tau_B \mathbf{E}_B + in_{xB\_} \tau_{B\_} \mathbf{E}_{B\_}, \tag{32}$$

where $\mathbf{E}_i = E_{xi}\hat{x} + E_{yi}\hat{y} + E_{zi}\hat{z}$ for $i = f, f\_, s, s\_, B$, and $B\_$ denote the polarization vectors of the rightgoing fast wave, leftgoing fast wave, rightgoing slow wave, leftgoing slow wave, rightgoing ion Bernstein wave, and leftgoing ion Bernstein wave, respectively. τ_i denotes the amplitude of the corresponding wave branch and n_{xi} is the x-component of the refractive index of that branch as calculated at the boundary. The amplitudes of n_{xi} are obtained most accurately by solving the full sixth-order WKB-limit dispersion relation from Eqs. (7) to (9) numerically. The assignment of the different n_{xi} to the modes is done according to the direction of energy flow so that the energy flux of the mode points outwards for outgoing and inwards for ingoing waves. If the n_{xi}^2 from the root finding is negative, indicating an evanescent mode and zero energy flux, we have demanded that the mode amplitude decays. In this representation there are 12 unknown τ_i's. Integration of the ordinary differential system (7)–(9) provides six relations between these unknowns. Six additional constraints must be provided in the form of boundary conditions.

2.5.2. *Boundary Conditions on the Short Wavelength Waves*

For the short wavelength modes ($i = s, s\_, B, B\_$), n_{xi} and the polarization components $\mathbf{E}_i$ can be determined from the WKB limit of Eqs. (7)–(9) [20]. These modes are usually damped in the plasma. Depending on the problem the short wavemodes may either be reflected at the boundary, propagating outward, or only propagating inward. The parallel wavenumber of the short wavelength mode is usually up- or downshifted in a toroidal geometry, resulting in strong damping when $k_{||}$ becomes large. This effect cannot be modelled in a plane geometry. There the damping of the short wavelength modes can be weak. To avoid this problem we assume only outgoing short wavelength modes. Our conditions impose $\tau_s = \tau_B = 0$ at the left endpoint at $x = 0$ and $\tau_{s\_} = \tau_{B\_} = 0$ at the right endpoint at $x = L$.

2.5.3. *Boundary Conditions on the Fast Wave*

We study the case where the incident wave comes from the low field side of the tokamak and propagates to the right. Because of this, we set $\tau_f = 1$ at the left boundary at $x = 0$. At the right boundary, $\tau_{f\_}$ gives the amplitude of the fast wave component reflected from the high field side outside of the calculation region and has to be determined as a function of τ_f defined at the right boundary. In the following we take $\tau_{f\_} = 0$ to simplify the analysis.

Because of the long wavelength of the fast wave branch and possible steep equilibrium gradients, n_{xf} and $n_{xf\_}$ at the endpoints cannot always be well estimated by the WKB approximation. Instead they can be calculated with the help of the Airy function solutions $F_\pm(z) = Ai(z) \pm iBi(z)$ of the wave equation around the endpoint [8]. The right going and left going waves are given by $+$ and $-$, respectively. $Ai(z)$ and $Bi(z)$ are the solutions to the Airy equation $E''_{yf} - zE_{yf} = 0$ with $z = -K_0^2/G^{2/3} + G^{1/3}(x - x_b)$. K_0 is defined by $K^2 = [(S - n_z^2)^2 - D^2]/(S - n_z^2)$ at the end point at $x = x_b$ according to $K^2 = K_0^2 - G(x - x_b)$ with $G = -d(K^2(x_b))/dx$. The solutions quoted above for F_+ and F_- are valid provided $K_0^2 > 0$ and $G > 0$. If $K_0^2 < 0$ and $G > 0$ we take $F_+(z) = Ai(z)$ for the right evanescent wave and

$F_-(z) = Bi(z)$ for the left evanescent wave. If $G < 0$ the solutions for right/left going waves should be interchanged. We then obtain $in_{xf} = (F'_+/F_+)\,G^{1/3}$ and $in_{xf_-} = (F'_-/F_-)\,G^{1/3}$. In the following, we approximate $n_{xf} = \sqrt{K_0^2}$ and $n_{xf_-} = -\sqrt{K_0^2}$ (or $n_{xf} = i\sqrt{-K_0^2}$ and $n_{xf_-} = -i\sqrt{-K_0^2}$, if $K_0^2 < 0$) which apply in the weak gradient limit. The difference between these two conditions is only a matter of definition of n_{xf} and n_{xf_-}.

The polarisations $\mathbf{E}_f$ and $\mathbf{E}_{f_-}$ of the fast wave branches are assessed from Eqs. (7)–(9) by simply making the substitutions $d/dx \to in_{xf}$ or in_{xf_-} in the equations.

2.5.4. *Boundary Conditions on* $\mathbf{E}$ *and* $d\mathbf{E}/dx$

Finally, by eliminating the three remaining unknown τ_i's from Eqs. (31)–(32) at each endpoint we find the boundary conditions on $\mathbf{E}$ and $d\mathbf{E}/dx$. The boundary conditions as described above have been chosen in order to be able to separate the wave field into a kinetic wave, a slow wave, and an incoming fast wave and a reflected fast wave at the endpoints. However, they are not exact due to the equilibrium gradients.

It is expected that the boundary conditions can be made more accurate if they are set at plasma regions with weak equilibrium gradients. In our examples in the previous section, the boundaries were placed at the steep gradient region. To demonstrate that the parasitic modes are excited, even when the boundary conditions are made to accurately match the outgoing plasma eigenmodes, we consider the model profiles

$$\begin{aligned} &\sigma = \sin(\pi x/2L) + i\rho_0 e^{-20x^2/L^2}; && -L \leqslant x \leqslant L \\ &\sigma = -1 + i\rho_0 e^{-20x^2/L^2}; && -5L/4 \leqslant x \leqslant -L \\ &\sigma = 1 + i\rho_0 e^{-20x^2/L^2}; && L \leqslant x \leqslant 5L/4, \end{aligned} \tag{33}$$

$S = \kappa\sigma$ and $D = -\kappa(\sigma + \alpha)$. We assume that $n_z = 0$, $E_y = 1$, $\kappa = 300{,}000$, $\rho_0 = 0.01$, $\alpha = 0.001$, and $L = 0.02$, and show E'_x calculated from Eq. (7) in Fig. 5. In this case, the dielectric tensor elements and their derivatives are continuous. The boundaries are placed at $x = \pm 5L/4$, where the boundary conditions are $E_x = -iDE_y/S + C_\pm$ and $E'_x = i\sqrt{\kappa}\,C_\pm$ and almost exactly match the outgoing plasma eigenmodes. In this case C_+ and C_- again are complex conjugates and $C_+ = -0.00187 - i0.00247$. By comparing the result with that in Fig. 4 we see an approximately fivefold reduction in the amplitude of the parasitic mode in the present case. The presence of the parasitic mode is obtained also for the undamped case $\rho_0 = 0$, where the boundary conditions exactly match the outgoing plasma modes and where $C_+ = -0.0026 - i0.001$, according to our calculations. Hence, we have proved that the short wavelength mode excitation can arise from the sole gradient effect in a finite interaction region and can exist even for accurately matched boundary conditions. The modes are parasitic if their origin lies in the failure of the FLR expansion leading to the nonphysical equilibrium gradients of the dielectric tensor elements or to the positive imaginary part of σ around the cyclotron resonances. We expect that this problem is not suppressed with the global boundary conditions discussed in the Introduction.

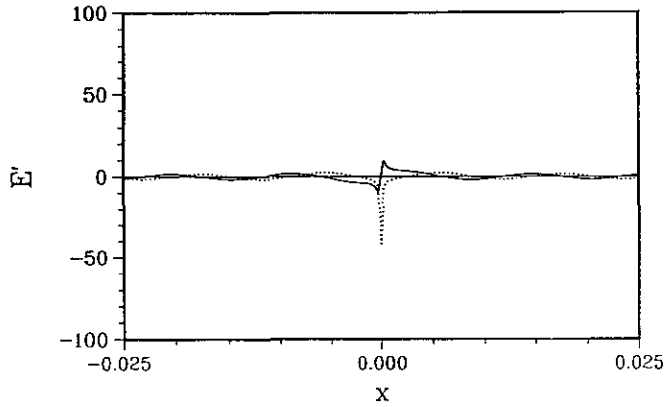

FIG. 5. $E'(x)$ calculated from Eq. (7) for the model profiles of σ, S, and D (see Eq. (33), and the text thereafter). The parameters are $n_z = 0$, $E_y = 1$, $\kappa = 300{,}000$, $\rho_0 = 0.01$, $\alpha = 0.001$, and $L = 0.02$.

3. THE NUMERICAL RESULTS

Solving Eqs. (7)–(9) with a cubic finite element method similar as in [3, 20] and using the above-mentioned boundary conditions we are able to calculate the conversion, reflection, and transmission coefficients for an incoming fast wave with sufficient accuracy and with reasonable computing time for routine runs. The energy flux I_{xi} of the ith mode is calculated from Eq. (29) for each mode using the mode amplitudes τ_i. We have $|R|^2 = -I_{xf_-}(0)/I_{xf}(0)$ for the fast wave reflection coefficient at the left boundary and $|T|^2 = I_{xf}(L)/I_{xf}(0)$ for the fast wave transmission coefficient.

3.1. Characteristics of Parasitic Coupling

To illustrate the effect of the polluting electrostatic modes, we consider a case in which the typical features can be clearly seen. The example comes from a simulation of ion cyclotron frequency minority ion heating in tokamak geometry. We take a deuterium minority in tritium with a concentration n_D/n_e of 50%. Here, n_e denotes the electron density and n_D is the deuteron density. The rest of the parameters are shown in Table I. The geometry for this case has been chosen so that within the slab there exist two different resonances. The cyclotron resonance layer of deuterium is located at about 10 cm from the left end. Due to the high minority concentration the fast wave is only weakly damped there. A few centimeters from the right boundary, there is the ion–ion hybrid resonance where

TABLE I

Parameters for the T(D)-Example

ω	$1.4325 \times 10^8\ s^{-1}$
n_y	0
n_z	2
B_0	3.0 T
R_0	3.0 m
$T_e = T_i$	5 keV
n_e	$5 \times 10^{19}\ m^{-3}$
n_D/n_e	0.5
n_T/n_e	0.5
L	0.75 m
R_{left}	3.1 m

$S - n_z^2 = 0$. Here the fast wave undergoes mode conversion to the ion Bernstein wave and is reflected back to the left while the remaining energy emanates from the right end in the form of a transmitted fast wave energy flux. The end points have been set so that both resonances can be considered isolated from the boundaries. At the left one, we use the boundary condition of an incoming fast wave mode and reflected fast and ion Bernstein modes. At the right one, the propagating modes are a transmitted fast wave and a converted ion Bernstein mode.

The behaviour of the solution is shown in Figs. 6 and 7. Figure 6 depicts both the radial electric field E_x and its derivative E_x', while Fig. 7 shows the absorption profile resulting from the numerical solution. The total energy flux components, i.e., the kinetic and Poynting energy fluxes, are also depicted in Fig. 7. In general, as long as the only mode present in the solution is the magnetosonic one, the radial field should be adiabatically coupled to the poloidal one, E_y, and thus exhibit a similar wavelength. In regions where an ion Bernstein mode exists due to either mode conversion, as on the right-hand side of the ion–ion hybrid resonance at $xc/\omega = 0.64$ m, or due to the wave mixing, it can be detected

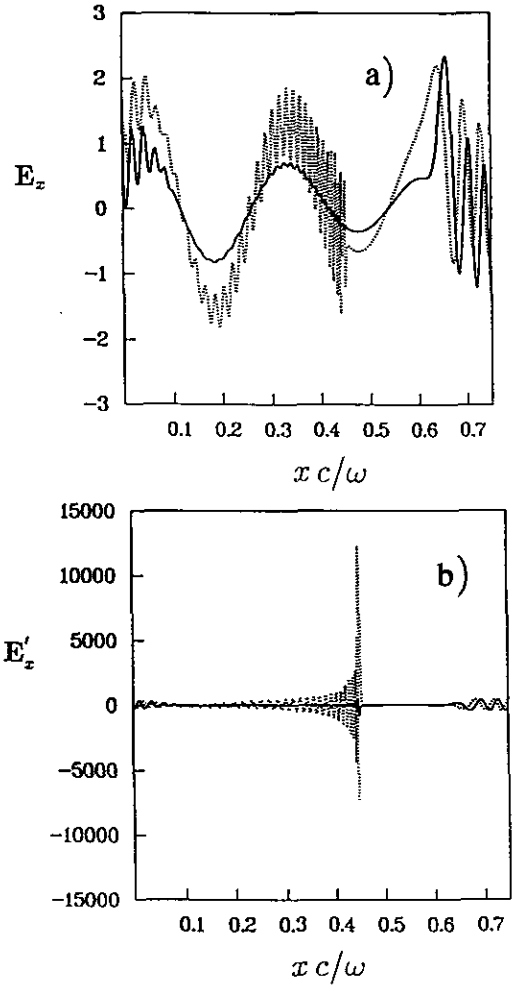

FIG. 6. (a) $E_x(x)$ calculated from Eqs. (7)–(9) for the example case of $T(D)$-heating. See Table I for the parameters. (b) The behaviour of E_x' in the example case.

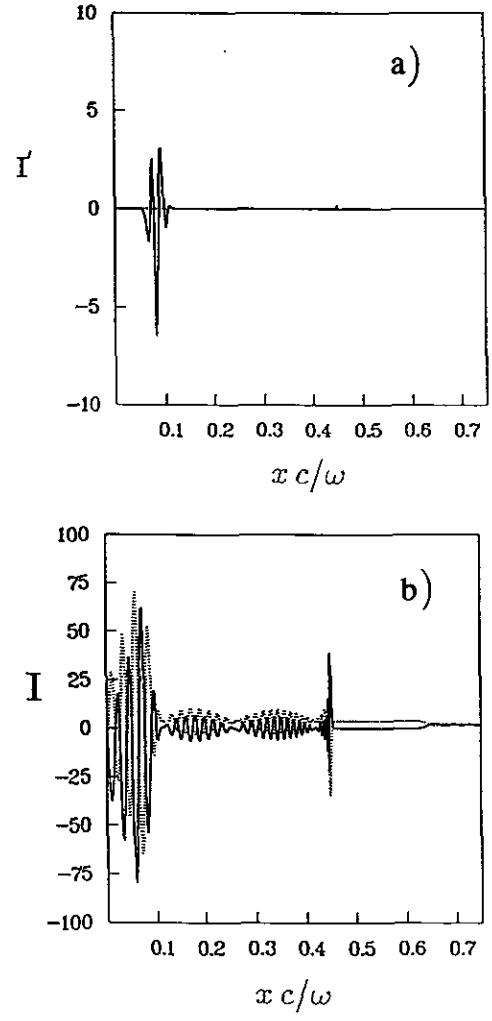

FIG. 7. (a) The absorption profile as calculated from the numerical energy flux for the case of Fig. 6. (b) The energy flux components: the kinetic (solid curve) and the Poynting fluxes (dotted) as a function of xc/ω in the case of Fig. 7a.

visually even at low levels by the strong fluctuations in E'_x. The indication of parasitic electrostatic waves can be found clearly everywhere in the left end of the slab, where $xc/\omega < 0.43$ m. At $xc/\omega = 0.43$ m, σ has a zero and the IBW, according to the dispersion given by the wave equations, becomes evanescent on the right-hand side of it [13]. The deleterious effects from the parasitic modes can be detected from the absorption profile (Fig. 7a). We find a region of negative absorption where the total energy flux increases as a function of x. Some fluctuations in the energy flux can be seen at the zero of σ, at which the parasitic ES mode is reflected back towards the cyclotron layer where it is created.

The theoretical predictions of the previous section, the parasitic coupling, and procedures for avoiding it can be compared more easily by excluding the zero of σ and studying a case with a separated cyclotron layer. In this way, one can check how the local dispersion of the electrostatic mode affects the creation of the polluting solution while still having the coupling between both components of the solution, E_x and E_y in the equations. Note that the zero of σ can be studied in a similar fashion. In the latter case, it is found that, although the mode created does lead to some numeri-

TABLE II

Parameters for Left Boundary for the Case Shown in Fig. 8a

	Inc. fast wave	Outg. fast wave	Outg. slow	Outg. IBW
n_{xi}	49.3	−49.3	−2938i	552
E_{yi}/E_{xi}	0.95i	0.95i	0.83i	−0.055i
$\tau_i E_{xi}$	1	0.005 − 0.006i	10^{-9}	0.139 − 0.26i
Energy flux	45.6	3×10^{-3}	0	−3.77
	$E_x = 1.14 - 0.27i$	$E_y = -0.008 + 0.95i$	$E'_x = 144 + 128i$	
	$\sigma = -0.066$	$\delta = 0.123$	$\sigma' = -0.123$	

Note. See Eqs. (31) and (32).

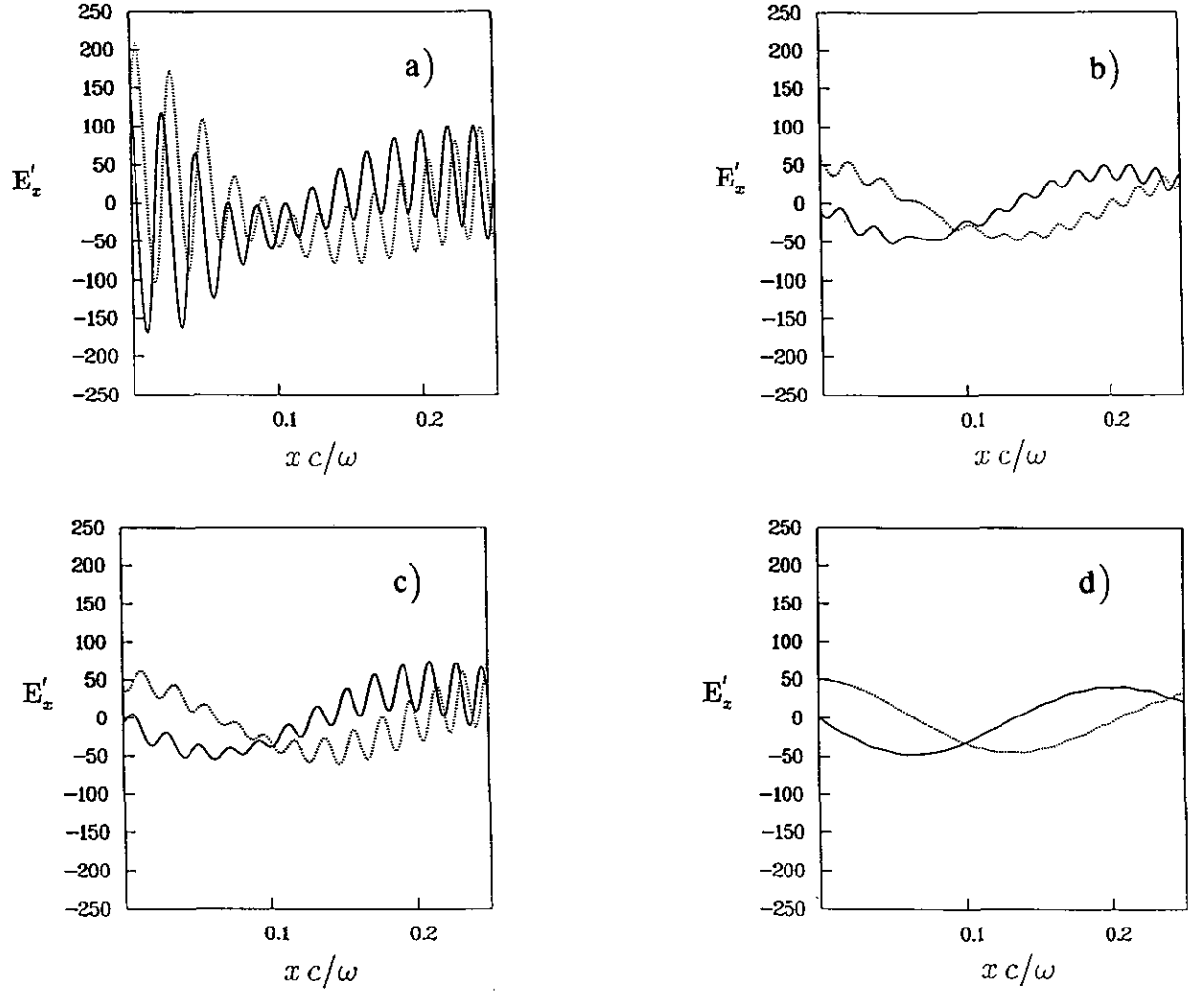

FIG. 8. (a) E'_x calculated from Eqs. (7)–(9) around the separated cyclotron resonance layer. Other parameters as in Table I and Figs. 6 and 7, except for the slab length which is 0.25 m ($R_{left} = 3.1$ m): solid curve, Re$[E'_x]$; dotted curve, Im$[E'_x]$. (b) As in Fig. 8a, but the imaginary parts of σ, σ', and δ are set to zero. (c) As in Fig. 8a, but with $-\delta$, σ' set equal to σ. (d) As in Fig. 8c, but, in addition, with the imaginary parts of δ, σ', and σ set to zero.

cal trouble at the vicinity of the zero, it has no real consequences on the solution, in terms of energy conservation.

Figures 8a to 8d show E'_x for a representative high concentration T(D)-case with the isolated cyclotron layer. We have chosen the location of the left boundary so that the cyclotron damping is very weak there. The right boundary has been set similarly but the zero of $\mathrm{Re}[\sigma]$ is left out. Four example calculations are depicted: one with the normal behaviour of σ, σ', and δ and showing some 8% of excess energy creation; one where the imaginary parts of σ, σ', and δ are set to zero; one in which σ' and $-\delta$ are set equal to σ; and the last one, in which σ' and $-\delta$ are set equal to σ and their imaginary parts are neglected. We provide in Table II the parameters for the boundary conditions at the left boundary to illustrate the result of Fig. 8a. To compare with the mode decomposition, one may take the parallel electric field as zero. From the various cases in Figs. 8a–8d one can see how these steps change the solution in the sense that energy conservation is improved and the amplitude of the pollution is greatly reduced. These show how, in accordance with the theoretical analysis in Section 2, the negative absorption can be simply avoided by setting the finite Larmor radius terms which originate from $n = 1$ terms (proportional to σ_1 and δ_1) to zero in the anti-Hermitian part of the dielectric tensor. A similar effect can be obtained by setting σ' and $-\delta$ equal to σ, which causes a comparable reduction in wave mixing. This is expected because the negative eigenvalue of the fast wave mode no longer exists with such a selection. The remaining wave mixing which can be clearly seen in Figs. 8b and 8c obviously originates from the steep gradients of σ, σ', and δ around the resonances as explained in Section 2. Figure 8d shows that the simultaneous symmetrization and real-valuedness of these terms has a beneficial effect in suppressing the wave mixing. In fact, a nearly complete suppression is found. This cannot be explained by the simplified analyses of Section 2. A more complete study, including both Eqs. (7) and (8) is needed to give a quantitative explanation. The absorption profiles corresponding to Figs. 8a and 8d can be simulated qualitatively in the WKB-limit by calculating the local absorption from two distinct FW and IBW modes integrated backwards from the left boundary, which shows, e.g., that the strong wave mixing encountered in the example of Fig. 8a can be connected with the wrong sign of the imaginary part of the IBW wave root.

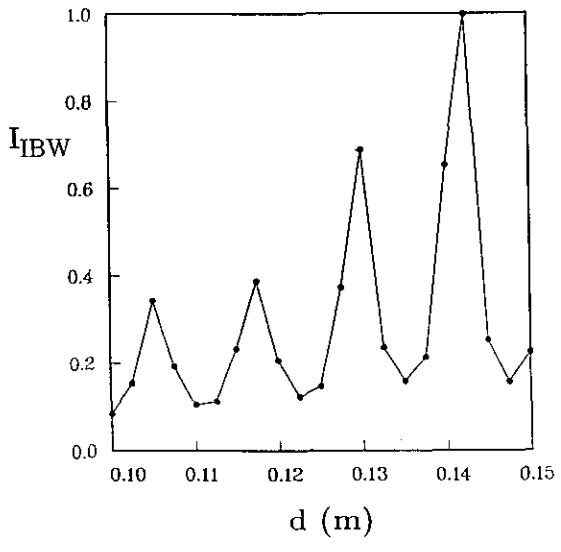

FIG. 9. The sum (I_{IBW}) of the reflected and transmitted IBW energy fluxes scaled with that of the incoming FW energy flux as a function of the location of the left end of the slab. We keep the right end at the same location and change the distance L between the left end and the resonance. Otherwise, we have the same parameters as in Fig. 8a.

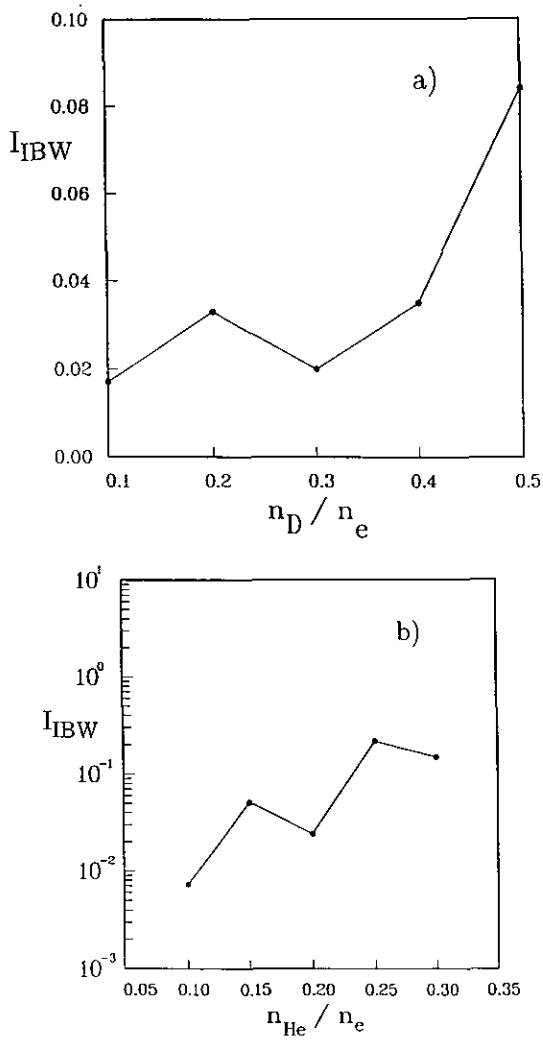

FIG. 10. (a) The sum of the left and right emanating IBW energy fluxes scaled with the incoming fast wave energy flux as a function of minority concentration (n_D/n_e) in a T(D)-case with parameters equal to those in Table I. (b) Pollution as defined in Fig. 10a as a function of $n_{^3He}/n_e$ for a case with ^{3}He in deuterium. Heating frequency $\omega = 1.91 \times 10^8$ 1/s corresponding to the ^{3}He cyclotron resonance at $R_0 = 3$ m for $B_0 = 3$ T. The electron density and plasma temperature are as in the T(D)-case; $n_z = 2$.

Although the examples shown in Figs. 6–8 are a clear indication of a high amplitude polluting mode, it should be noted that it need not be so in the general case. The creation of the polluting mode follows from the anomalous, unphysical dispersion located around the zero or singularity of the real part of σ and can thus be reduced by affecting the local behaviour of σ by simply changing the parameters for the calculation. We next discuss the dependence of the wave mixing on the parameters with the geometry of an isolated cyclotron resonance, as in Fig. 8. Note that with the modifications discussed in the context of that figure, the polluting conversion can be reduced to very low levels in the following examples.

How the wave mixing depends on the location of the boundaries is shown in Fig. 9, where the ratio of the energy flux of the parasitic mode to that of the incident magnetosonic mode is shown as a function of the distance d between the left end of the slab and the cyclotron resonance. The other parameters are kept unchanged with respect to those in Fig. 8a. For d increasing from 10 to 15 cm, the left-going parasitic mode shows an oscillatory growth with the small scale oscillations having a wavelength of the ion Bernstein mode. If d is further increased, the effect of the boundary conditions on the parasitic coupling becomes more complicated as the phase of the fast wave begins to play a role at large enough d. The oscillation is in accordance with the analysis in Section 2, where we found the parasitic mode excitation to be strongly dependent on d.

The minority concentration, ion composition, and density all have an effect on the strength of the conversion that leads to wave mixing. This is demonstrated in Figs. 10 to 12, where we show the relative wave mixing in terms of IBW energy flux creation as a function of minority density, plasma density, and parallel refractive index n_z for the T(D) heating scheme considered earlier and for the case with helium-3 in deuterium (D(^{3}He)). The general trends are clear: by increasing the concentration of the resonant minority the pollution becomes worse because the ratio

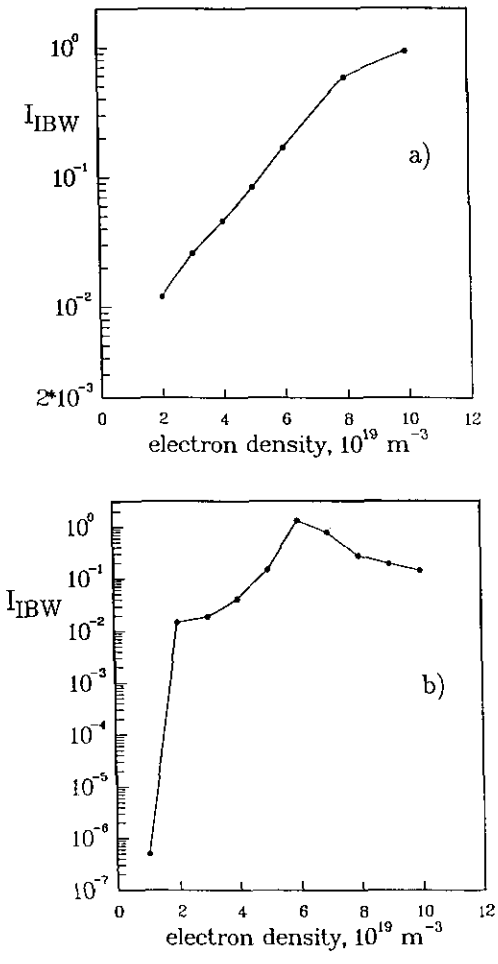

FIG. 11. (a) The wave mixing as a function of plasma density for the T(D)-case. The parameters are equal to those in Table I. (b) The wave mixing as a function of the density in the D(^{3}He)-case. The parameters are given in Fig. 10b; $n_{^3He}/n_e = 0.3$.

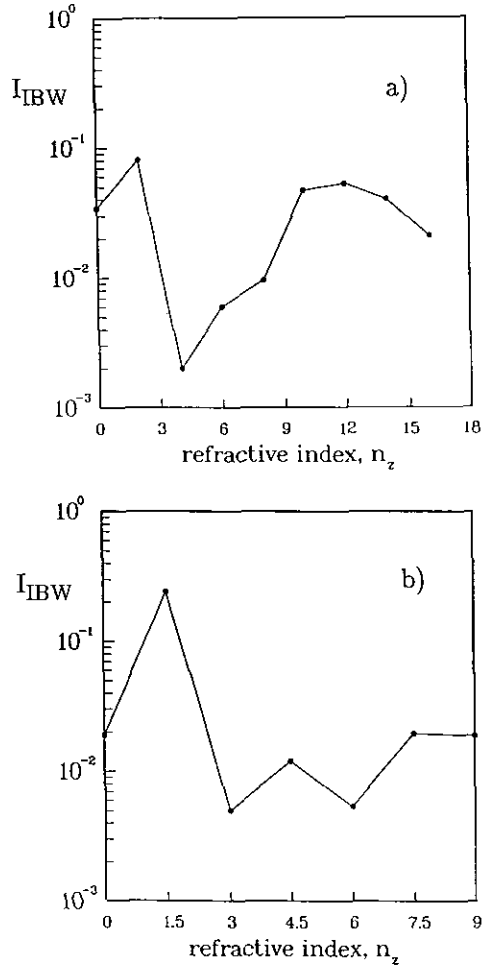

FIG. 12. (a) The wave mixing as a function of n_z for the T(D)-case. The parameters are equal to those in Table I. (b) The wave mixing as a function of n_z in the D(^{3}He)-case. The parameters are given in Fig. 10b; $n_{^3He}/n_e = 0.3$.

between $|E_-|$ and $|E_+|$ and the imaginary part of σ increase with the minority density which in its turn increases the negative absorption. Also, the spatial behaviour of the real part of σ changes. A similar effect can be seen from Fig. 11 as a function of plasma density. The dependence of parasitic coupling on the parallel refractive index n_z does not display strong features, as shown in Fig. 12, except for the fact that the coupling seems to be maximized at low n_z.

The role played by the wave mixing in a case involving also the ion–ion hybrid resonance is more complicated due to the FW reflection from the hybrid resonance layer. The latter changes the behaviour and magnitude of E_y at the cyclotron resonance. Also, the reflection of the electrostatic mode from the zero of σ may be of importance. However, from Figs. 10 to 12 we make the conjecture that in the case of D(^{3}He) studies, in particular, and at low minority concentrations, the existence of wave mixing may be forgotten in the sense that the results are still physically meaningful.

3.2. How to Avoid Unphysical Effects

To be able to use the simple second order wave equations (7)–(9) and to be sure that they describe correctly the wave absorption, propagation, and scattering, special methods are needed. On the basis of the previous results we are guided to change the dispersion relation in the neighborhood of the cyclotron resonances, so that the excitation of wave mixing is reduced to a sufficiently low level. There are several possible practical approaches to this goal. A method has already been shown in action in Fig. 8, which demonstrated how by modifying the finite Larmor radius corrections σ, σ', and δ the amplitude of the polluting mode can be reduced. We note that this kind of choice has been used by Brambilla [20] in analyzing the antenna coupling for ion Bernstein wave heating. Similarly, one could omit the fundamental contributions completely, which results in equations of the form used by Colestock and Kashuba [21]. This would, however, affect the physics of mode conversion at the ion–ion hybrid resonance.

One question that must be asked is how the absorption of the fast magnetosonic wave is perturbed at the cyclotron layer if one changes the imaginary part of the thermal corrections and perhaps also the real part, too. The magnitude of the change can be estimated from Eq. (30) qualitatively by comparing the absorption due to Im S and Im D to that resulting from the thermal corrections σ, δ, and σ'. Thus we obtain, e.g., the ratio

$$\mathrm{Im}[\sigma]\,|E_x'|^2/\mathrm{Im}[S]\,|E_x|^2 \simeq k_f^2 r_{\min}^2, \qquad (34)$$

where k_f is the fast wavenumber at the resonance and $r_{\min}$ is the minority Larmor radius. For the fast wave, this ratio is typically small. Hence, by setting the imaginary part of σ to zero the magnitude of the fast wave transmission over the resonance is not affected strongly. A similar conclusion can be drawn about the damping of the fast and the ion Bernstein modes in the vicinity of the hybrid resonance. To avoid altering the transit time damping or the second harmonic absorption and to avoid changing the IBW dispersion relation, we propose setting $\mathrm{Im}\,\lambda_1 = 0$ in σ, δ, and σ' and the definition $\delta = \delta_2 - \delta_1$ and $\sigma' = 2\lambda_0 + \sigma_2 - \sigma_1$ so as to eliminate the parasitic coupling.

Recently, Chow *et al.* [13] have studied the dispersion relation around the zero of $\mathrm{Re}[\sigma]$ between the cyclotron resonance and the ion–ion hybrid resonance in the case of D(^{3}He) minority heating. They also note the spurious short wavelength mode appearing on the low field side of this zero and present a clever modification to σ to correct the dispersion. An analogous method could possibly be found to each particular application in our case, too, but it would make a general purpose code rather complicated.

Table III compares the energy fluxes of the outgoing waves for the case of T(D)-heating including the ion–ion hybrid resonance (see again Table I for parameters) for various methods of suppressing wave mixing discussed earlier in the case of an isolated cyclotron layer on the basis of Fig. 8. We have defined $\Delta I = \int Q\,dx$ for the total absorption. Of the results, one can see how the wave mixing, in general, has a very small effect on the mode-converted IBW at the right end and on the transmitted fast wave. This is due to the fact that the resonance and mode conversion layers are separated from each other by the second zero of $\mathrm{Re}[\sigma]$. The IBW is evanescent between this zero and the hybrid resonance. In all cases, the applied changes have a reducing effect on the wave mixing. In this particular example the additional gain from setting $\mathrm{Im}[\lambda_1]$ to zero, together with the symmetrization, is quite small, in which context one should, however, remember the fairly large differences seen in Fig. 8. Note that it is necessary to apply the changes to all of σ, σ', and δ and not only to the first of these, as one could expect from the single equation analysis of Section 2. In 1D global codes, it has been popular [3, 14] to add a phenomenological damping term $i\rho$ to the first coefficient of Eq. (7). The goal of artificial damping is in such cases to take into account damping processes not included or to avoid the free

TABLE III

Reflected, Converted and Transmitted Mode Energy Fluxes Scaled with the Incident Fast Wave (FW) Energy Flux with Different Modifications to the Kinetic Corrections

	refl. FW	refl. IBW	transm. FW	conv. IBW	ΔI
No modifications	0.886	0.318	0.044	0.041	−0.289
Real σ, σ', δ	0.877	0.0005	0.044	0.041	0.038
$\sigma' = -\delta \leftarrow \sigma$	0.908	8×10^{-8}	0.045	0.043	0.004
$\sigma = \sigma' = -\delta \leftarrow \mathrm{Re}[\sigma]$	0.912	5×10^{-8}	0.043	0.040	0.005

Note. See Table I for the parameters.

propagation of the ion Bernstein modes that are created through mode conversion at the ion–ion hybrid resonance. In a real situation such waves can be damped by mechanisms that are not present in a slab model such as an upshift of the $k_{||}$ which increases absorption or stochastic damping. According to our analysis, the inclusion of an $i\rho$-type term reduces the pollution, too, provided that the magnitude and the profile of ρ are properly chosen. However, this method, as well as the others described above, does not eliminate the pollution completely and the modifications in the absorption profile are inevitable.

4. CONCLUSIONS

The appearance of unwanted phenomena in the solution of the plasma wave propagation has usually been attributed to the failure of the specific numerical approach used. In this paper we have shown that there exists another reason for the emergence of pollution, understood in this paper in the generalized sense of mixing the original or expected solution with other modes of any origin. Here, the origin lies in the breakdown of the physical assumptions used for the derivation of the plasma response in the wave equations. Through the mechanism of the gradient-driven mode conversion, enhanced by negative absorption, the original mode couples to the short wavelength mode allowed by the wave equations, which in the examples studied here leads to the generation of polluting ion Bernstein waves.

The strength of the generation of pollution depends on the plasma composition. The critical parameters are the relative concentration of the resonant minority ions and the density. They determine the conversion both by setting the magnitude of the imaginary parts of the important resonant terms in the dielectric tensor elements at the cyclotron layer and by affecting the behaviour of the real part in the same way. The value of the parallel refractive index n_z, on the other hand, has an effect through the fact that at high values of n_z the zeros of $\mathrm{Re}[\sigma]$ cease to exist and through the $|E_+|/|E_-|$ ratio.

We have presented a specific method to change the wave equations so as to reach a correct description of the absorption of the fast magnetosonic wave and of the mode conversion process occurring at the ion–ion hybrid resonance, where the FLR expansion is valid. Applied to an example they show that the strength of the polluting mode can be reduced to a satisfactory degree. Similarly, they point out that in global wave codes the problem of wave mixing might remain at a relatively low level, given an extra damping mechanism for the ion Bernstein wave that is similar to those applied in some of the existing codes. We would, however, like to stress that our approach seems to be easier to apply in practice, even in global codes. The removal of the parasitic modes is in any case a goal which ought to be reached, in order to make this problem solvable within the differential equation formulation.

ACKNOWLEDGMENTS

The authors thank Dr. L.-G. Eriksson and Professor J. Pitkäranta for useful comments during this work. M. A. would like to thank the Jenny and Antti Wihuri Foundation, the Heikki and Hilma Honkonen Foundation, and the National Research Council for Technology, the Academy of Finland for financial support.

REFERENCES

1. For the many existing 2D codes see, e.g., L. Villard, K. Appert, R. Gruber, and J. Vaclavik, *Comput. Phys. Rep.* **4**, 95 (1986); A. Fukuyama, K. Itoh, and S. Itoh, *Comput. Phys. Rep.* **4**, 137 (1986); E. F. Jaeger, D. B. Batchelor, H. Weitzner, and H. Whealton, *Comput. Phys. Commun.* **40**, 33 (1986); D. Edery and H. Picq, *Comput. Phys. Commun.* **40**, 95 (1986); D. N. Smithe, P. L. Colestock, R. J. Kashuba, and T. Kammash, *Nucl. Fusion* **27**, 1319 (1987); B. A. Carreras, V. E. Lynch, E. F. Jaeger, D. B. Batchelor, and J. S. Tolliver, *J. Comput. Phys.* **88**, 183 (1990).
2. The 1D case is discussed in the FD formulation most comprehensively in E. F. Jaeger, D. B. Batchelor, and H. Weitzner, *Nucl. Fusion* **28**, 53 (1988).
3. K. Appert, T. Hellsten, J. Vaclavik, and L. Villard, *Comput. Phys. Commun.* **40**, 73 (1986) gives a good review over the application of FEM to plasma wave propagation.
4. K. Appert, T. Hellsten, J. Vaclavik, and L. Villard, *Comput. Phys. Commun.* **30**, 1195 (1988).
5. X. Llobet, K. Appert, A. Bondeson, and J. Vaclavik, *Comput. Phys. Commun.* **59**, 199 (1990).
6. T. H. Stix, *The Theory of Plasma Waves* (McGraw–Hill, New York, 1962).
7. M. Brambilla and T. Krücken, *Nucl. Fusion* **28**, 1813 (1988).
8. T. H. Stix and D. G. Swanson, in *Handbook of Plasma Physics, Vol. 1*, edited by A. A. Galeev and R. N. Sudan (North-Holland, Amsterdam, 1983), Chap. 2.4.
9. O. Sauter and J. Vaclavik, in *Theory of Fusion Plasmas, Proc. of Joint Varenna–Lausanne Int. Workshop, Varenna, Italy, August 27–31, 1990*, edited by E. Sindoni, F. Troyon, and J. Vaclavik, pp. 403–419.
10. M. Brambilla, *Plasma Phys. Controlled Fusion* **33**, 1029 (1991).
11. O. Sauter, J. Vaclavik, and F. Skiff, *Phys. Fluids B* **2**, 475 (1990).
12. M. J. Alava and J. A. Heikkinen, *Phys. Fluids B* **4**, 9 (1992).
13. C. Chow, V. Fuchs, and A. Bers, *Phys. Fluids B* **2**, 1089 (1990).
14. M. Brambilla, *Plasma Phys. Controlled Fusion* **31**, 723 (1989).
15. T. Martin and J. Vaclavik, *Helv. Phys. Acta* **60**, 471 (1987).
16. J. A. Heikkinen and M. J. Alava, *Plasma Phys. Controlled Fusion* **33**, 397 (1991).
17. M. J. Alava and J. A. Heikkinen, *Phys. Scripta* **45**, 345 (1992).
18. S. Ichimaru, *Basic Principles of Plasma Physics* (Benjamin/Cummings, London, 1980), p. 89.
19. F. Skiff, M. Ono, P. Colestock, and K. L. Wong, *Phys. Fluids* **28**, 2433 (1985).
20. M. Brambilla, Rep. IPP 5/15, Max-Planck Institute fur Plasmaphysik, Garching, 1987'(unpublished).
21. P. Colestock and R. Kashuba, *Nucl. Fusion* **23**, 763 (1983).